



Effect of surface morphology on the sputtering yields. II. Ion sputtering from rippled surfaces

Maxim A. Makeev ^{*}, Albert-László Barabási

Department of Physics, University of Notre Dame, Notre Dame, IN 46566, USA

Received 20 August 2003; received in revised form 16 February 2004

Abstract

Off-normal ion bombardment of solid targets with energetic particles often leads to development of periodically modulated structures on the surfaces of eroded materials. Ion-induced surface roughening, in its turn, causes sputtering yield changes. We report on a comprehensive theoretical study of the effect of rippled surface morphology on the sputtering yields. The yield is computed as a function of the parameters characterizing the surface morphology and the incident ion beam, using the Sigmund's theory of ion sputtering. We find that the surface morphology development may cause substantial variations in the sputter yields, depending on a complex interplay between the parameters characterizing the ripple structure and the incident ion beam. For certain realizations of the ripple structure, the surface morphology is found to induce enhanced, relative to the flat surface value, sputtering yields. On the other hand, there exist regimes in which the sputtering yield is suppressed by the surface roughness below the flat surface result. We confront the obtained theoretical results with available experimental data and find that our model provides an excellent qualitative and, in some cases, quantitative agreement with the results of experimental studies.

© 2004 Elsevier B.V. All rights reserved.

PACS: 68.35.C; 34.50.D; 81.65.C; 79.20.R

1. Introduction

Ion-bombardment of solid targets is known to cause the formation of periodically modulated structures (often referred to as ripples) on the surfaces of eroded materials. The phenomenon of

ripple formation was discovered and studied experimentally nearly three decades ago [1–3]. Recently, a revival of interest in the ripple formation has been observed in connection with various technologically motivated applications of the ion-sputtering [4–16]. The sputter erosion is of particular interest due to its extensive use in a variety of applications related to the surface analysis, such as secondary ion mass spectroscopy (SIMS), Auger electron microscopy (AES) and X-ray photoelectron spectroscopy (XPS). Although significant progress has been made in understanding the interaction of energetic particles with solid targets [17–21], a number of unresolved

^{*} Corresponding author. Present address: Collaboratory for Advanced Computing and Simulations, Department of Materials Science and Engineering, University of Southern California, VHE 608, 3651 Watt Way, Los Angeles, CA 90089-0242, USA. Tel.: +1-213-821-2661; fax: +1-213-821-2664.

E-mail addresses: makeev@usc.edu (M.A. Makeev), alb@nd.edu (A.-L. Barabási).

problems remain. Those include the issues related to the sputtering yield changes in SIMS and, associated with these changes, significant depth profile degradation. In the light of technological importance of the SIMS, a number of experimental as well as theoretical studies focused on the problem of surface morphology effects on the sputter yields. As experimental studies have shown, the ion-beam-induced ripple morphology is responsible for the changes that occur in the sputtering yields during the sputter erosion process [4–16]. Thus, for a better control of these important experimental technique, one has to either find a way to predict the sputtering yield changes or suppress the roughness development. An accurate correction procedure, accounting for the yield changes in the SIMS, was not developed up to date due to a complex character of the problem (i.e. complex mechanisms determining the surface morphology, in the first place, and the existing interplay between these mechanisms and the sputtering yield changes). Consequently, the major bulk of experimental studies concentrated on the methods, which allow for roughness suppression. Zalar was the first to suggest that the surface depth profile resolution can be improved by sample rotation [4]. Subsequently, he showed that the main reason for the observed significant improvements in the depth resolution is the suppression of surface morphology development by sample rotation during the ion bombardment [5]. The first study, quantifying the effect of the surface ripple structures on the sputtering yields, was reported by Stevie et al. [6], who demonstrated that the sputtering yield changes are directly correlated with the *onset of the ripple morphology development*. Similar conclusions on the connection between the sputtering yield changes and the ripple morphology development were later drawn by Wittmaack [7,13], who, among all, put forward a simple semi-heuristic model of ion sputtering from targets with non-planar (faceted) surfaces. This model allowed him to conclude that the sputtering yield changes can be understood on the basis of yield variations with the local impact angle [7]. Experimental studies, performed by Karen et al. [11,12,15] further quantified the effect of ripple structures on the sputtering yields. Moreover, in

[11,12,15], the temporal evolution of the sputtering yield has been studied in the process of sample rotation, providing a clear evidence that the ripple morphology development (or suppression) constitutes the major factor, which defines the sputtering yield behavior in the process of ion bombardment. Experimental investigations of the effect of sample rotation on the ripple structures prompted theoretical efforts aimed to describe this phenomenon. Based upon Bradley and Harper theory of ripple formation [22], a theoretical model explaining the effect of sample rotation on the ripple morphology was proposed by Bradley and Cirilin [23]. Subsequently, Carter has shown that the combined effects of sample rotation and rocking can further suppress the ripple structure development, thus leading to even greater improvement in the depth profile resolution [24].

Although there exists an ample experimental evidence that the surface roughness development causes considerable variations in the sputtering yields [6–16], there is no consistent theory, which would account for this effect. Indeed, the classical theoretical literature, focusing on the ion sputtering, is based upon the flat surface approximation, thus ignoring the surface roughness [17–21]. In this article, we present a detailed account of our model of ion sputtering from surfaces with sinusoidal ripple morphology, aimed to predict the effect of surface ripples on the sputtering yield. A short account of the model was previously given in [25]. Here, we expand the scope of discussion to various aspects of the problem. In the framework of our model, we regard the rippled surfaces as periodically modulated structures, fully characterized by the amplitude of periodic modulations and the wavelength, thus neglecting the fluctuations in shape of the surface ripples. To compute the sputtering yields, we employ the well known Sigmund's theory of ion sputtering, which was modified to incorporate the ripple morphology of the surfaces. This theory was proven to work reasonably well for amorphous targets, in the intermediate and high primary ion energy regimes [20,21]. A combination of analytical and numerical methods is used to investigate the behavior of the yield as a function of the parameters characterizing the surface roughness (such as the amplitude of peri-

odic modulations and the ripple wavelength) and primary ions (such as the incident ion energy, the angle of incidence and the widths of the deposited energy distribution). We find that the ripple morphology can both enhance and suppress the yield, depending on the interplay between the parameters characterizing the surface ripple morphology and the ion bombardment process. Our results allow us to make rather specific predictions regarding the effect of the surface roughness on the yield. Thus, we show that the surface roughness induced increase in the sputtering yields may exceed 100% (in agreement with the previously reported experimental findings [6,7,11]). Moreover, we directly confront the predictions of our theory with available experimental data, finding that our model offers results in an excellent qualitative and, in some cases, quantitative agreement with the experiments in many aspects of the problem.

The rest of the article is organized as follows. In Section 2, we discuss experimental results on the sputtering yield changes, taking place during the ion-erosion of surfaces with ripple morphology. Next, in Section 3, we present an overview of theoretical models, describing the ripple formation process. This is followed by a brief overview of the Sigmund's theory of ion-sputtering, presented in Section 4. Further, in Section 5, we provide a detail account of our model, including derivation of the integral equation for the sputtering yield and discussion of the methods of its solution. In this section, we also present derivation of an analytical form, approximating the yield function behavior in the limiting case of small ripple amplitudes. Section 6 is fully devoted to discussion of the obtained results. Further, in Section 7, we compare our results with the existing experimental data on behavior of the sputtering yields from the rippled surfaces. Finally, in Section 8, we briefly summarize our principal findings.

2. Experimental results

Zalar was the first to correlate the sputtering yield changes, taking place during surface depth profiling, with the onset of ripple structure development [4,5]. Subsequently, a number of experi-

mental studies reporting on the ion-eroded surface morphology development and, associated with it, sputtering yield changes, appeared in the literature. In this section, we briefly overview the major experimental results, which are focused on the effect of ripple morphology induced sputtering yield changes. These results will provide us with necessary guidance in developing the theoretical approach and allow to validate the principal findings obtained in the framework of our theoretical model.

The ripple structure development and, associated with it, sputtering yield changes, were studied by Stevie et al. [6], in experiments with 6-, 8-keV O_2^+ and 14.5-keV Cs^+ -ion bombardment of Si surfaces. Additionally, the morphology evolution of GaAs surfaces was studied using 2.5-, 5.5- and 8-keV O_3^+ and 14.5-keV Cs^+ primary ions. The employed primary ion angles of incidence were varied in the range between 39° and 52° . It was shown that the sputtering yields demonstrate an enhancement by nearly 70%, as compared to the flat surface value, for 6 keV O_2^+ -ion bombarded Si surfaces, while the same, nearly 70%, enhancement in the sputtering yields were observed in the case of 8-keV O_2^+ primary ion bombarded GaAs surfaces. The morphology of the ion-sputtered surfaces for both Si and GaAs samples was monitored in the process of erosion using SEM and development of ripple structures was observed in the cases, when the sputtering yield changes occurred. Similarly, the ripple formation on silicon surfaces, accompanied by corresponding changes in the sputtering yields and depth profile degradation was reported by Wittmaack [7,13]. He studied initially flat Si samples bombarded with 10-keV O_2^+ primary ions, incident at the angles ranging from 0° to 75° . It was found that the ion bombardment causes ripple structure formation, provided the primary ion angles of incidence lie between 32° and 58° . Depending on the angle of incidence (taken within the range, where the ripple structures were formed), the sputtering yields were found to demonstrate substantial variations, with the largest deviations from the flat surface results observed for $\theta = 45^\circ$. On the basis of his experimental findings, Wittmaack [7] suggested that the sputtering yield changes are related to the surface

morphology development and put forward a simple model, based upon the yield variations with the local impact angle, to give a quantitative account of the effect. Further investigations of the phenomenon of ripple formation were performed by Cirlin et al. [9], who studied sputter depth profiles of GaAs and AlGaAs superlattice surfaces, using 7-keV O_2^+ primary ions. The ripple structure development, accompanied by nearly 40% rise in the sputtering yields, was observed in each case. The surface morphology was analyzed using SEM. It was found that the ion bombardment induces a periodically modulated structures on the target surfaces, with ripple wavelength $\lambda \simeq 75$ nm, for both GaAs and AlGaAs. No changes in the ripple wavelength were observed to occur with the increasing sputtered depth (sputtered time). Moreover, ion sputtering experiments with sample rotation were also performed. These studies have unambiguously shown that the sample rotation inhibits the ripple formation and, in this case, no changes in the sputtering yields take place. Karen et al. [11,12] studied the oxygen-ion-induced ripple structures, formed during depth profiling of GaAs surfaces, using scanning tunneling microscopy (STM). The authors reported on the abrupt yield changes taking place at a certain sputtered depth, and correlated them with the onset of ripple morphology development. The surface morphology evolution in the process of ion bombardment was studied, and a monotonic increase in the ripple amplitude, h_o , with the sputtered depth up to a certain point was observed, with subsequent stabilization of h_o at a constant value. The steady-state ripple amplitude was estimated as $h_o \simeq 30$ – 50 nm. On the other hand, the wavelength of the ripple structure remained nearly constant in the process of ion-erosion, with the estimated value of λ being $\simeq 230$ nm. An extensive experimental study of the ripple formation process on ion-bombarded Si surfaces and, associated with it, sputtering yield changes were performed by Vajo et al. [16], using O_2^+ primary ions. The incident ion energies were varied in the range from 1 to 9 keV, while the angle of incidence was kept constant at 40° . It was found that the ripple structures are formed on the target's surfaces in the course of ion-erosion, with the ripple wavelength being nearly proportional to the

incident ion energy and ranging from 95 to 408 nm. The ripple wavelength was observed to remain constant up to a certain sputtered depth, d , dependent on the incident angle. In the region of large values of d , λ was observed to increase nearly linearly with d . The rate of growth was found to be strongly dependent on the primary ion energy. The secondary ion intensities were found to be proportional to the incident ion flux. It was shown that the sputtering yield behavior with the sputtered depth can be understood fairly well within the framework of the Wittmaack's model (see [7]).

In summary, obtained experimental results allow to conclude that the ion sputtering, under certain experimental conditions, leads to ripple formation. The process of formation of the ripple structures on the ion-eroded surfaces is accompanied by the sputtering yield changes and degradation in the depth profile resolution. For a number of materials, the ripple formation occurs if the energy of incident ions exceeds the value of a few keV and the angles of incidence lie between 30° and 60° . In the process of ripple structure development, the ripple amplitude grows exponentially with time (sputtered depth), while the ripple wavelength remains largely independent of d . If the ion sputtering is continued for longer times, a nearly linear growth in the ripple wavelength with the sputtered depth is observed. The magnitudes of the secondary ion intensities are found to be proportional to the incident ion flux.

3. Theory of ripple formation

A theoretical explanation of the phenomenon of ripple formation on the ion-eroded surfaces of amorphous materials was suggested by Bradley and Harper (BH) [22]. Using the Sigmund's theory of ion-sputtering, the authors have shown that the local surface curvature dependent preferential erosion, acting during ion bombardment, may induce an instability, which leads to the formation of periodically modulated structures on the ion-eroded surfaces. The instability arises as a result of different erosion rates for troughs and crests, the former being eroded faster than the latter. At elevated temperatures, this instability is balanced by

thermally activated surface diffusion [26,27]. Consequently, the physical characteristics of the obtained steady-state ripple morphology are defined by the interplay between these two processes. A brief overview of the theory is as follows. In the absence of overhangs, a surface profile can be described by a single valued height function $h(x, y, t)$, measured from an initially flat configuration, which is taken to lie in the (x, y) plane. We chose the ion beam direction parallel to the xOz plane, forming an angle $0 \leq \theta < \pi/2$ with the z -axis. By projecting the normal component of the erosion velocity onto the z -axis, we obtain the following equation for the surface profile evolution:

$$\frac{\partial h(x, y, t)}{\partial t} \simeq -v(\theta) + v_x \nabla_x^2 h(x, y, t) + v_y \nabla_y^2 h(x, y, t) - K \nabla^4 h(x, y, t), \quad (1)$$

where $v(\theta)$ corresponds to the erosion velocity of a flat surface, v_x and v_y are the effective surface tension coefficients and $K = D\gamma\Omega^2 n/k_B T$ is the relaxation rate due to thermally activated surface diffusion, $D = (v_o/k_B T) \exp(-E_a/k_B T)$ [26,27], γ is the surface free energy, Ω is the atomic volume, E_a is the activation energy for surface diffusion, v_o is the vibrational frequency of surface atoms, $k_B T$ is temperature (in energy units), and n is the areal density of surface atoms. The time evolution of the amplitude of periodic modulations is given by $|h(k, t)|^2 = h_i(k)^2 \exp(rt)$, where h_i is an initial surface roughness and r is the growth rate of the ripple structure. By employing the linear stability analysis, applied to Eq. (1), the following expression for the growth rate r can readily be obtained:

$$r = -(Ja/n)Y_o(\theta)\{v_x k_x^2 + v_y k_y^2 + K(k_x^2 + k_y^2)^2\}, \quad (2)$$

where J is the incident ion flux, $Y(\theta)$ is the angular dependence of the yield from a flat surface, a is the penetration depth and n is the density of atoms of the target material. Moreover, the linear stability analysis demonstrates that, for small values of k , the modes are unstable and the fastest growing mode, which determines the ripple wavelength, is given by

$$\lambda = 2\pi/k_c = \sqrt{\frac{2K}{|v|}} \sim (JT)^{-1/2} \exp\left\{-\frac{E_o}{k_B T}\right\}, \quad (3)$$

where v is the largest in absolute value of the two negative surface tension coefficients, v_x and v_y . As the further analysis of Eq. (1) shows, the ripple orientation is defined by the angle of incidence: for small θ the ripples are oriented parallel to the ion direction, while for large θ they are perpendicular to it.

Comparison of the BH theory with experimental data was performed by Mayer et al. [28], who have shown that the spectrum of spatial frequencies and the kinetics of ripple formation are in qualitative agreement with the BH model, provided the stochastic roughening term is included. In general, the BH theory predicts well the ripple wavelength and the orientation. On the other hand, a number of limitations of the theory were reported on in the literature too. Thus, the inclusion of a viscous relaxation term in Eq. (1) was shown to result in suppression of the high frequency components, leading to the inhibition of the ripple structure development in this regime [28,29]. Moreover, Eq. (1) is linear and predicts an unbounded exponential growth for the ripple amplitude. Thus, it cannot account for the stabilization of the ripples and for the kinetic roughening, both phenomena being strongly supported by the experiments [16,30]. To explain within a single theory all the experimentally observed morphologies, recently the BH theory has been extended to incorporate the non-linear effects and the randomness in the incident ion flux [31,32]. The non-linear theory predicts the stabilization of the ripple amplitude, due to a complex interplay between the linear and non-linear terms in the equation of surface morphology evolution. Moreover, it demonstrates the possibility of coexistence, at different length scales, of kinetic roughening and the ripple formation. Furthermore, the low-temperature behavior of the ripple wavelength, reported in the literature, clearly shows that there are other than thermally activated relaxation mechanisms, driving the ripple formation in the low-temperature regime [3]. Such mechanism, based upon the ion-induced effective smoothing, was recently suggested in [33], and further developed in [32]. A number of studies have been focused on the effect of oxygen concentration as the major driving force of the ripple formation process [34,35]. As subsequent studies have shown, however, the

ripple formation process cannot be explained merely on the basis of chemical composition variations [36].

4. Theory of ion sputtering

Ion bombardment of solids with energetic particles causes the erosion of target material's surfaces. The erosion rate is characterized by the sputtering yield, Y , defined as the average number of atoms leaving the surface of a solid per incident particle. The theory of ion sputtering, based upon the microscopic considerations of the processes taking place in the bulk of the bombarded material, was developed by Sigmund [20,21]. Making use of the hypothesis that the sputtering yield of a polycrystal (amorphous material) can be calculated by assuming random slowing down throughout the cascade, he derived a general expression for the yield as a function of the ion-target and target-target cross-sections as well as atomic binding energies in the bulk of the target material and on the surface. One of the practically important results obtained by Sigmund is the deposited energy distribution function, which was found to have the Gaussian form

$$E(\mathbf{r}_\perp, z) = \frac{\epsilon}{(2\pi)^{3/2} \sigma \mu^2} \exp \left\{ -\frac{z^2}{2\sigma^2} - \frac{x^2 + y^2}{2\mu^2} \right\}. \quad (4)$$

Here, ϵ is the kinetic energy of an incident ion, σ and μ are the widths of the deposited energy distribution along the z - (chosen parallel to the incident ion beam direction) and x (y)-axis, respectively. The parameters σ and μ are material dependent and vary with the physical properties of the target material and the incident ion energy. Deviations of the deposited energy distribution from the Gaussian form (see Eq. (4)) occur mainly when $M_1 \geq M_2$, where M_1 is the mass of the projectile and M_2 is the mass of the target material atom. As was shown in the theoretical studies by Sigmund [20,21] and Winterbon [37], the electronic stopping (i.e. the inelastic scattering) does not affect much the shape of deposited energy distribution. Moreover, subsequent Monte Carlo sim-

ulations of the sputtering process validated both the deposited energy and the damage distribution forms [17–19]. Comparison of the predictions of the Sigmund's theory of ion sputtering with experimental results have shown that the theory describe well the qualitative behavior of the sputtering yields and, in many cases, a good quantitative agreement was found. In general, computation of the sputtering yield, using Eq. (4) requires a knowledge of the mean path of an incoming ion, traveling inside the bulk of a target material (often referred to as penetration depth). It was shown that the penetration depth can be expressed in terms of the parameters characterizing the target material and the incoming ion energy as follows:

$$a(\epsilon) = \frac{1-m}{2m} \gamma^{m-1} \frac{\epsilon^{2m}}{nC_m}. \quad (5)$$

Here, n is the target atom density, γ is a constant of the order of unity, C_m is a constant dependent on the parameters of the interatomic interaction potential [20] and $m = m(\epsilon)$ is a factor, which varies slowly from $m = 1$, at high energies, to $m = 0$, at very low energies. It must be emphasized that, in the region of intermediate energies, i.e. for intermediate and large values of ϵ , $m = 1/2$, and the penetration depth behavior with the incoming ion energy can be approximated well by the linear dependence, $a(\epsilon) \sim \epsilon$. Note that, in general, the deposited energy distribution is defined by the energy deposition depth and not the penetration depth, a . On the other hand, these quantities are of the same order of magnitude and, therefore, in the following, we assume that the estimates for a can be used to approximate the energy deposition depth.

In the framework of the Sigmund's theory of ion sputtering, the local yield from a target material surface element ds can be computed using

$$Y(\mathbf{r}) ds = AE(\mathbf{r}) ds, \quad (6)$$

where $Y(\mathbf{r}) ds$ is the total number of the target atoms leaving the surface element ds , located at a distance \mathbf{r} on the target material's surface from the point of impact of the projectile, and $E(\mathbf{r})$ the energy deposited by the incoming ions, taken per

unit volume at a point \mathbf{r} . The material constant A depends on the surface binding energy and the scattering cross-sections [20,21], the exact expression being

$$A = \left\{ \frac{3}{4\pi^2} \right\} \frac{1}{U_o C_o n^2}, \quad (7)$$

where U_o is the surface binding energy and C_o is a constant proportional to the square of an effective inter-atomic interaction potential. Thus, the knowledge of the material constants, the penetration depth and the widths of deposited energy distribution allows one to compute the sputtering yields for an arbitrary target material. Such calculations, for the flat surfaces, were performed, for instance, in [20] and shown to provide a reasonable description of the sputtering process. It should be noted, however, that, despite the fact that the Sigmund's theory is known to describe adequately various aspects of the ion sputtering, it also has well known limitations. The most important of such limitations are listed below.

- (a) The theory was derived for amorphous materials and may not provide a fully adequate description of the crystalline targets.
- (b) The assumption of random slowing down and of arbitrary collisions works satisfactory only

at the intermediate and high energies $\epsilon \sim 1\text{--}100$ keV, while it breaks down at the low energies.

- (c) The surface binding energy, U_o , brings in a number of uncertainties, which may affect the quantitative results of the theory. Thus, it may undergo a significant changes in the process of ion-erosion, caused by the ion-induced amorphization of the near-surface regions of the target material and by the changes in the local surface chemistry in these regions.

5. Theoretical approach

5.1. General expression for the yield

The physical process taking place during the ion bombardment of solid targets with energetic particles, is illustrated schematically in Fig. 1. An incoming ion strikes the sinusoidal target surface at point O , penetrates the target's interior and stops at a distance a , at point P , after all its kinetic energy is dissipated due to the elastic and non-elastic interactions with the atoms of the target material. The energy deposited by an incoming ion is distributed in the interior of the target material and the near-surface region. The transfer of the

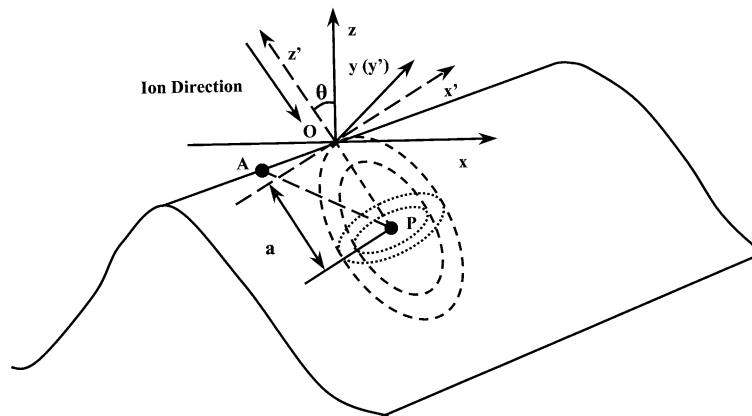


Fig. 1. Schematic illustrating the assumed system. Following a straight trajectory (solid line), the ion hits the sinusoidal surface, penetrates an average distance a inside the solid (dotted line), spreading out its kinetic energy and stops at point P . The deposited energy decreases with the distance from the point P following Gaussian, the dotted ellipses in the figure indicating schematically the equal energy contours. The energy, released at point P , contributes to the erosion rate at the point A on the surface. In the schematic, (x', y', z') correspond to the local coordinate frame, while (x, y, z) denotes the laboratory frame of coordinates.

deposited energy to an arbitrary point A on the target material surface causes the erosion, characterized by the erosion velocity (or the erosion rate), v . Below, we derive the general expression for the erosion velocity in the local coordinate frame (x', y', z') . We define the local reference frame as follows: the z' -axis is chosen to be parallel to the direction of the incident ion beam, while the x' - and y' -axis are located in the plane perpendicular to it. The x' -axis is chosen in such a way as to have the ion trajectory being confined to the $x'Oz'$ plane. In the local coordinate frame, the surface profile is given by $z' = h'(x', y')$. In Fig. 1 we also show the laboratory frame (x, y, z) , defined as follows: the z -axis is chosen parallel to the average surface orientation, while the x - and y -axis lie in the plane perpendicular to it. The scattering events, caused by an incoming ion, take place in the region of the target material with characteristic length a_e , which is the average energy deposition depth (usually, it is of the order of the penetration depth). Following the Sigmund's theory [20,21], we assume that the energy deposited at an arbitrary point A on the surface by an incoming ion can be approximated by the Gaussian distribution, Eq. (4), and the local erosion rate of the target surface is proportional to the energy deposited at the point A by all bombarding ions. Since there are many incoming ions, reaching the targets' surface per unit time (the number of ions per second, per surface area is called fluence and is one of the controlled parameters in experiments involving the ion bombardment), the erosion rate at the point A is expressed as

$$v = \Lambda \int_{\mathcal{R}} d\mathbf{r}'_{\perp} E(\mathbf{r}'_{\perp}, h'(x', y')) \Phi(\mathbf{r}'_{\perp}, h'(x', y')). \quad (8)$$

Here, the integration is performed over the region R , covering all points at which the deposited energy contributes to the erosion rate at a generic point A on the surface, and $\mathbf{r}'_{\perp} = (x', y')$. The function $\Phi(\mathbf{r}'_{\perp}, h'(x', y'))$ accounts for the corrections to the uniform incident ion flux J , due to the local surface curvature. In our choice of the local reference frame, the incoming ion flux has only x' - and z' -components, i.e. it is confined in the $x'Oz'$ plane of the local coordinate frame. The most general expression for the local flux, for surfaces

with non-zero local curvature, can be represented by the following form:

$$\Phi(x', y', h'(x', y')) = J \cos\{\arctan(\nabla'_x h'(x', y'))\}. \quad (9)$$

Fig. 2 illustrates the calculations of the ion flux function from simple geometrical considerations. In the figure, θ is the primary ion angle of incidence taken with respect to the normal to the average surface orientation, i.e. the z -axis of the laboratory frame of coordinates. The angle $\phi = \arctan(\nabla'_x h'(x', y'))$ defines the correction to the angle between the local normal \mathbf{n} to the surface and the primary ion beam, which arises due to the local surface curvature. Now, it is straightforward to obtain the expression for the sputtering yield, which can be used to compute the yields from an arbitrary surface with a non-planar geometry given by $h'(x', y')$ in the local coordinate frame. Indeed, in the most general form, the yield is given by

$$Y = \frac{vn}{\langle J \rangle}, \quad (10)$$

where n is the density of the target atoms and $\langle J \rangle$ is the average incident ion flux, $\langle J \rangle = \langle \Phi(x', y', h'(x', y')) \rangle$. For sinusoidal surface profile, the averages $\langle \dots \rangle$ in Eq. (10) are taken over one period

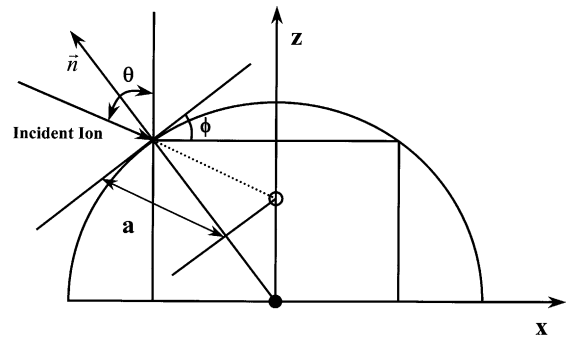


Fig. 2. Schematic illustrating the coordinate transformation. An ion arrives to the target material surface at an angle, θ , taken with respect to the local normal to the surface, \mathbf{n} . Due to the local surface curvature, there is an angle, ϕ , between the local normal to the surface, \mathbf{n} , and the z -axis of the laboratory frame. From simple geometrical considerations, we readily obtain the transformation, Eq. (14), for the local curvature dependent ion flux.

of the surface modulations and the unit of length along the $y(y')$ -direction, for each realization of the periodically modulated surface. It can readily be performed by integrating Eq. (9) over one period of modulations, while the erosion velocity is given by Eq. (8), and n is a material dependent constant.

5.2. Rippled surfaces

Neglecting the fluctuations in the shape of the ripples, a ripple structure can well be approximated by the following height function (in the laboratory coordinate frame):

$$h(x) = h_o \cos(2\pi x/\lambda). \quad (11)$$

To calculate the yields from the rippled surfaces, we employ the set of Eqs. (8)–(10), combined with the expression for the deposited energy distribution. Thus, the total yield at an arbitrary point (x'_o, y'_o) on the surface with sinusoidal profile (see Eq. (11)), measured in the local coordinate frame (x', y', z') , is given by

$$Y(x'_o, y'_o) = \frac{\Lambda n \epsilon}{(2\pi)^{3/2} \sigma \mu^2 \langle J \rangle} \times \int_{-\infty}^{\infty} \int_{-\infty}^{\infty} dx' dy' \Phi(x', y', h'(x')) \times \exp \left\{ -\frac{(a - h'(x') - h'(x'_o))^2}{2\sigma^2} - \frac{(x' - x'_o)^2}{2\mu^2} - \frac{(y' - y'_o)^2}{2\mu^2} \right\}. \quad (12)$$

Note that, with our choice of the local coordinate frame (x', y', z') , the ion flux is confined to the $x'Oz'$ plane. Consequently, the most general expression for $\Phi(x', y', z'(x', y'))$, which takes into account the local surface curvature, has the following form:

$$\Phi(x', h'(x')) = J \cos \left\{ \arctan \left(\frac{\partial h'(x', y')}{\partial x'} \right) \right\}. \quad (13)$$

To obtain an analytical expression for the yield in the *laboratory reference frame*, we perform a transformation of the coordinate system from the

local frame to the laboratory one (see Fig. 2). If we define the primary ion angle of incidence with respect to the z -axis (laboratory frame) as θ , such a transformation is a simple rotation in the xOz plane, given by

$$\begin{aligned} x' &= x \cos \theta + h(x) \sin \theta, \\ h' &= -x \sin \theta + h(x) \cos \theta, \end{aligned} \quad (14)$$

where $h(x)$ is the sinusoidal surface profile, given by Eq. (11). In order to obtain the experimentally measurable total yield, we average Eq. (12) over the period of surface modulations, λ , and unit length along the y -direction, L_o . This gives the following expression for the average sputtering yield:

$$Y = \frac{1}{\lambda L_o} \int_0^\lambda \int_0^{L_o} dx_o dy_o Y(x_o, y_o). \quad (15)$$

By combining Eqs. (12)–(15), we obtain the final expression for the yield as

$$\begin{aligned} Y &= \frac{F}{\lambda} \int_0^\lambda \int_{-\infty}^{\infty} dx dx_o \cos \left[\arctan \left(\theta - \left(\frac{\partial h}{\partial x} \right) \right) \right] \\ &\times \exp \left\{ -\frac{\Gamma_1(x - x_o)^2}{a^2} \right\} \\ &\times \exp \left\{ -\frac{\Gamma_2(h(x) - h(x_o))^2}{a^2} \right\} \\ &\times \exp \left\{ -\frac{\Gamma_3(x - x_o)(h(x) - h(x_o))}{a^2} \right\} \\ &\times \exp \left\{ -\frac{\Gamma_4(x - x_o)}{a^2} \right\} \\ &\times \exp \left\{ -\frac{\Gamma_5(h(x) - h(x_o))}{a} \right\}. \end{aligned} \quad (16)$$

In the following, we assume linear relations between the deposited energy distribution widths and the penetration depth (deposited energy depth): $\sigma = \epsilon_1 a$ and $\mu = \epsilon_2 a$, where ϵ_1 and ϵ_2 are constants less than 1. Using these assumptions, the factor F in Eq. (16) can be cast in the following form:

$$F = \frac{\Lambda n \epsilon a}{(2\pi) \mu \sigma \langle J \rangle} \exp(-1/2\epsilon_1^2), \quad (17)$$

while the coefficients Γ_i ($i = 1-5$) are given by

$$\begin{aligned}\Gamma_1 &= \frac{1}{2} \left(\frac{\sin^2 \theta}{\epsilon_1^2} + \frac{\cos^2 \theta}{\epsilon_2^2} \right), \\ \Gamma_2 &= \frac{1}{2} \left(\frac{\cos^2 \theta}{\epsilon_1^2} + \frac{\sin^2 \theta}{\epsilon_2^2} \right), \\ \Gamma_3 &= \frac{1}{2} \left(\frac{1}{\epsilon_2^2} - \frac{1}{\epsilon_1^2} \right) \sin \theta \cos \theta, \\ \Gamma_4 &= \frac{1}{\epsilon_1^2} \sin \theta, \\ \Gamma_5 &= -\frac{1}{\epsilon_1^2} \cos \theta.\end{aligned}\quad (18)$$

The average flux, $\langle J \rangle$, is

$$\langle J \rangle = \frac{J}{\lambda} \int_0^\lambda dx \cos \left\{ \theta + \arctan \left(\frac{2\pi h_o}{\lambda} \sin \left(\frac{2\pi x}{\lambda} \right) \right) \right\}.\quad (19)$$

Eqs. (16)–(19) can be analyzed numerically, for a given set of parameters characterizing the surface morphology and the primary ion beam. The analysis is performed in Section 6.

5.3. Small amplitude expansion

In the preceding section, we have derived a general expression for the sputtering yield, which allows for calculating the total sputtering yields as a function of the experimentally relevant parameters characterizing the primary ion beam and the eroded surface roughness. The expression was obtained in an integral form and can be employed to obtain numerical solutions only. In some limiting cases, however, we can deduce an exact analytical form for the yield function. The relevance of this form to experiments is discussed below in the course of derivation. We proceed as follows.

(i) As experimental studies of the ripple formation indicate, the ratio of the ripple amplitude to wavelength, h_o/λ , is a small quantity [11,16]. Consequently, we can always expand Eq. (19) in powers of the small parameter $\partial h/\partial x \sim h_o/\lambda$ and keep terms up to the second order

only, obtaining the following approximate expression for the average ion flux:

$$\langle J \rangle = J \cos \theta \left\{ 1 - \frac{1}{4} \left\{ \frac{2\pi h_o}{\lambda} \right\}^2 \right\}.\quad (20)$$

(ii) Although the experimentally relevant range of the ripple amplitude variations can be much larger than the average penetration depth, the initial stages of the process of ripple formation correspond to small values of h_o/a ratio. Thus, in order to reveal the behavior of the yield function in the initial stages of ripple formation, we can expand Eq. (16) in powers of the small parameters (h_o/a) and (h_o/λ), keeping, again, the terms up to the second order only. The details of the series expansions, in both λ/a and h_o/a are given in Appendix A, the final expression being

$$\begin{aligned}Y &= F \exp \left\{ \frac{\Gamma_4^2}{2\Gamma_1} \right\} \sqrt{\frac{\pi}{\Gamma_1}} \\ &\times \left\{ 1 + \left(\frac{h_o}{a} \right)^2 \left(Y_1 + \tan(\theta) \left(\frac{2\pi}{\lambda} \right) Y_2 \right) \right\},\end{aligned}\quad (21)$$

where the Y_1 and Y_2 terms are given by

$$\begin{aligned}Y_1 &= \left(\frac{\Gamma_5^2}{2} - \Gamma_2 - \frac{1}{2} \Gamma_3 \Gamma_5 + \frac{\Gamma_3^2}{4\Gamma_1} + \frac{\Gamma_3^2 \Gamma_4^2}{8\Gamma_1^2} \right) \\ &+ \left(\cos \left(\frac{\pi \Gamma_4}{\lambda \Gamma_1} \right) \exp \left\{ - \left(\frac{2\pi}{\lambda} \right)^2 \frac{1}{4\Gamma_1} \right\} \right) \\ &\times \left(-\frac{1}{2} \Gamma_5^2 + \Gamma_2 + \frac{\Gamma_3 \Gamma_4 \Gamma_5}{2\Gamma_1} - \frac{\Gamma_3^2}{4} \sqrt{\frac{\pi}{\Gamma_1}} \right) \\ &\times \left(1 - \left(\frac{2\pi}{\lambda} \right)^2 \frac{1}{4\Gamma_1} - \frac{\Gamma_3^2 \Gamma_4^2}{8\Gamma_1^2} \right) \\ &+ \left[\sin \left(\frac{\pi \Gamma_4}{\lambda \Gamma_1} \right) \exp \left\{ - \left(\frac{2\pi}{\lambda} \right)^2 \frac{1}{4\Gamma_1} \right\} \right] \\ &\times \left(-\frac{\pi \Gamma_5 \Gamma_3}{\lambda \Gamma_1} + \frac{\pi \Gamma_3^2 \Gamma_4}{2\Gamma_1^2 \lambda} \right).\end{aligned}\quad (22)$$

$$Y_2 = \frac{1}{2} \exp \left\{ - \left(\frac{2\pi}{\lambda} \right)^2 \frac{1}{4\Gamma_1} \right\} \\ \times \left[\sin \left(\frac{\pi\Gamma_4}{\lambda\Gamma_1} \right) \left(\frac{\Gamma_3\Gamma_4}{2\Gamma_1} - \Gamma_5 \right) + \frac{\Gamma_3\pi}{\lambda\Gamma_1} \cos \left(\frac{\pi\Gamma_4}{\lambda\Gamma_1} \right) \right]. \quad (23)$$

The coefficients Γ_i ($i = 1-5$) are given by Eq. (18), and $\bar{\lambda} = \lambda/a$.

(iii) In the case of normal incidence, $\theta = 0$, Eqs. (21)–(23) can readily be reduced to

$$Y = \frac{\Lambda n \epsilon}{(2\pi)\epsilon_2\epsilon_1 a} \exp(-1/2\epsilon_1) \sqrt{2\pi\epsilon_2^2} \\ \times \left\{ 1 + \left(\frac{1}{2\epsilon_1^4} - \frac{1}{2\epsilon_1^2} \right) \left(\frac{h_o}{a} \right)^2 \right. \\ \left. \times \exp \left[- \frac{2(\pi\epsilon_2)^2}{\bar{\lambda}^2} \right] \right\}. \quad (24)$$

Note that the sputtering yield for flat surfaces can readily be obtained from Eq. (24) by taking $\lambda \rightarrow \infty$ and/or $h_o \rightarrow 0$ limits.

6. Results and discussion

In this section, we present our results on the sputtering yield behavior, obtained by means of numerical analysis of the set of Eqs. (16)–(19). The parameters and the ranges of their variations for both the ripple structure and the incident ion beam have been judiciously chosen on the basis of available experimental data. The ripple characteristics, such as the ripple amplitude and the wavelength, are measurable in experiment quantities and have been previously reported in the literature (see Section 2). On the other hand, the estimates for the penetration depths (deposited energy depths), for different materials and incident ion types as a function of the incident ion energy are normally obtained from Monte Carlo simulation of the high energy impact processes [39]. In our model, we adopt the following values for normalized widths of the deposited energy distribution: $\epsilon_1 = 1/2$ and $\epsilon_2 = 1/4$. This choice of parameters corresponds to an asymmetric deposited energy

distribution with $\sigma = a/2$ and $\mu = a/4$, where a is the incident ion penetration depth (deposited energy depth). This choice is consistent with the results, obtained in the computer experiments on the high energy impacts modeling [17–19].

As experimental studies show (see Section 2 for details), in the initial stages of the ripple formation process, the ripple amplitude, h_o , grows exponentially with the erosion time (or sputtered depth), while the ripple wavelength remains nearly constant. Consequently, plotting the sputtering yield as a function of the ripple amplitude, for fixed values of the ripple wavelength and the penetration depth, we obtain all the essential information on the sputtering yield temporal variations, taking place due to the ion-induced ripple morphology development and evolution. Note, however, that, as observed in experiments, there always exists a critical value of h_o , at which the ripple amplitude stabilizes at a nearly constant value [16,30]. Furthermore, in the real systems, the ripple structure initiation is known to occur at a certain value of the sputtered depth, d_o . These observations should be carefully taken into account, when our model calculations are compared with experimental data. In Fig. 3, the normalized yield, $Y(h_o)/Y(0)$, is plotted as a function of the amplitude of periodic modulations, h_o . Note that $Y(0)$ correspond to the flat surface results for a given angle of incidence, θ_i . The yield behavior was studied for fixed values of the penetration depth, $a = 5$ nm, and the ripple wavelength, $\lambda = 200$ nm. Different curves in the figure correspond to different values of θ_i . In general, two characteristic regimes in the yield behavior can be distinguished depending on h_o . For small values of the ripple amplitude, the yield rapidly increases with h_o . This behavior holds for all considered values of θ_i . As the value of h_o increases further, however, the yield passes through a maximum and then becomes a decreasing function of the ripple amplitude. The decreasing with h_o yields are observed in Fig. 3 for all considered angles of incidence, except for $\theta_i = 0^\circ$ (open squares in Fig. 3). In the case of normal incidence, the yield function increases with a slower rate, never reaching the maximum value within the range of considered ripple amplitudes. Both the position of the peak and its magnitude depend

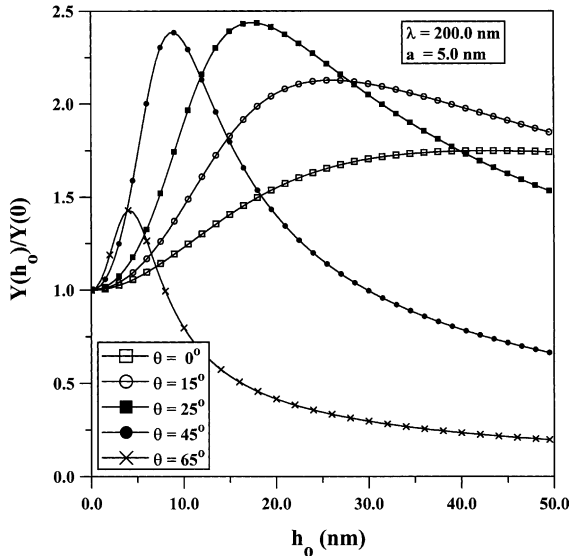


Fig. 3. Normalized yield, $Y(h_o)/Y(0)$, is plotted as a function of the amplitude of periodic modulation, h_o , for fixed values of the ripple wavelength, $\lambda = 200.0$ nm, and the penetration depth, $a = 5.0$ nm. Different curves in the figure correspond to different values of the angle of incidence, θ : (1) $\theta = 0^\circ$ (open squares); (2) $\theta = 15^\circ$ (open circles); (3) $\theta = 25^\circ$ (solid squares); (4) $\theta = 45^\circ$ (solid circles); (5) $\theta = 65^\circ$ (crosses). The solid lines are drawn to guide the eye.

strongly on the angle of incidence. Thus, for small values of θ_i , the largest observed deviation from the flat surface results, $[Y(h_o) - Y(0)]$, increases with θ_i , and reaches the maximum value at $\theta = 45^\circ$. In the range of angles $\theta \geq 45^\circ$, the peak value of the yield function start to decrease, with the minimum deviations from the flat surface result observed for $\theta_i = 65^\circ$. The position of the peak shifts towards large values of h_o , as θ_i increases. Furthermore, in the limit of large h_o and for values of θ_i exceeding 45° , the yield is considerably suppressed, decreasing below the flat surface limit (see the curves corresponding to $\theta_i = 45^\circ$ and $\theta_i = 65^\circ$, in Fig. 3). The point of transition from the enhanced to suppressed yield moves towards larger values of h_o , as θ_i decreases. The smallest value of h_o , at which such transition occurs, is observed for $\theta_i = 65^\circ$.

In the limit of small values of (h_o/a) ratio, Eqs. (16)–(19) can be expanded in powers of (h_o/a) . This gives an analytical form describing the yield

function behavior in the initial stages of the ripple formation process. The form is given by Eq. (21). The yield functions, obtained via numerical solution of the set of Eqs. (16)–(19) for different values of the roughness and incident ion parameters, have been previously fitted using Eq. (21) and found to follow closely the h_o^2 dependence in the initial stages of surface roughness development [25]. Note that qualitatively similar behavior was obtained for the sputtering yields from random (self-affine) surfaces, in which case the yield was found to vary as w_{sat}^2 with the width of rough surfaces [40,41]. Furthermore, as we show in Section 7, Eq. (21) provides highly accurate estimates for the yield behavior in a surprisingly wide range of the ripple amplitude variations.

To further our understanding of the effect of the ripple morphology on the yield, in Fig. 4, we show the normalized yield, $Y(h_o)/Y(0)$, as a function the ripple amplitude, for fixed values of the penetration depth, $a = 5$ nm, and the angle of incidence,

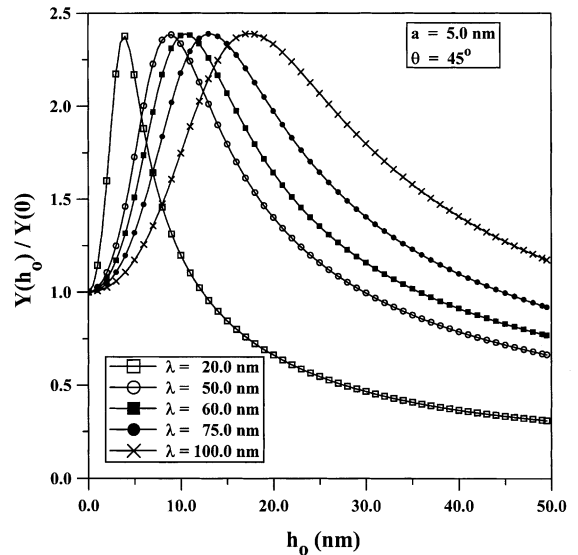


Fig. 4. Normalized yield, $Y(h_o)/Y(0)$, is plotted as a function of the amplitude of the periodic modulation, h_o , for fixed values of the incidence angle, $\theta = 45^\circ$, and the penetration depth, $a = 5.0$ nm. Different curves in the figure correspond to different values of the ripple wavelength: (1) $\lambda = 20.0$ nm (open squares); (2) $\lambda = 50.0$ nm (open circles); (3) $\lambda = 60.0$ nm (solid squares); (4) $\lambda = 75.0$ nm (solid circles); (5) $\lambda = 100.0$ nm (crosses). The solid lines are drawn to guide the eye.

$\theta = 45^\circ$. Different curves in the figure correspond to different values of the ripple wavelength, λ . In the region of small ripple amplitudes, the yield demonstrates a rapid increase with h_o , following $\sim h_o^2$ dependence. In all considered cases, at a certain value of h_o , the yield reaches a maximum, and then undergoes a fall-off, in the regime of large ripple amplitudes. The positions of the maximum are strongly dependent on the value of the ripple wavelength, with the peak position, h_o^p , shifting to the region of larger ripple amplitudes for larger values of λ , following approximately $h_o^p = B\lambda$ relation, with magnitude of B being between 1/6 and 1/7. The magnitudes of the maximum deviation of the yield from the flat surface result are approximately the same in all considered cases of the ripple wavelengths, being $\simeq 240\%$. For small, as compared to the ripple amplitude, values of λ , in each considered case there exist a wide region of h_o values over which the yield is suppressed by the ripple morphology (see Fig. 4 (open squares and open circles)). We note that, in experiments on ion sputtering of surfaces with developed ripple morphology, the ripple wavelength is always much greater than the ripple amplitude. Consequently, the suppression of the yield has never been observed experimentally for major chemical constituents of the sputtered materials. On the other hand, it is known that other surface morphologies may cause suppression of the yield below flat surface result [42]. This emphasizes the importance of adequate description of the surface roughness for the problem of sputtering yield computations.

As experimental studies of the ion-induced ripple formation demonstrate, the ripple wavelength is a function of a number of parameters, including the temperature, incident ion range in the target material, and the material properties [16]. Thus, it can vary substantially for different materials and sputtering conditions. Moreover, it was observed that, under certain sputtering conditions, it increases with the sputtered depth in the long sputtered times limit [16]. Given that a universal ripple wavelength does not exist and it may vary substantially during the erosion process, the dependence of the sputtering yield on the ripple wavelength warrants more detailed investigation. We compute the yield dependence on the ripple

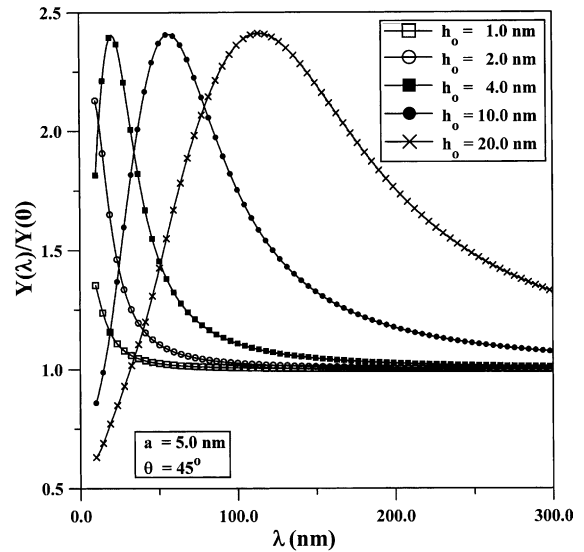


Fig. 5. Normalized yield, $Y(\lambda)/Y(0)$, is plotted as a function of the ripple wavelength, λ , for fixed values of the angle of incidence, $\theta = 45^\circ$, and the penetration depth, $a = 5.0$ nm. Different curves in the figure correspond to different values of the ripple amplitude: (1) $h_o = 1.0$ nm (open squares); (2) $h_o = 2.0$ nm (open circles); (3) $h_o = 4.0$ nm (solid squares); (4) $h_o = 10.0$ nm (solid circles); (5) $h_o = 20.0$ nm (crosses). The solid lines are drawn to guide the eye.

wavelength, for different values of the parameters characterizing the incident ion beam and the ripple structure. In Fig. 5, we show the dependence of the sputtering yield on the ripple wavelength, computed for fixed values of the penetration depth, $a = 5$ nm, and the angle of incidence, $\theta = 45^\circ$. Different curves in the figure correspond to different values of the ripple amplitude. The yield functions are normalized to the flat surface result at $\theta = 45^\circ$. As implicit in Fig. 5, the behavior of the yield with λ differs considerably for different values of h_o . When $h_o < a$, the yield is a decreasing function of λ in the whole region of λ variations. In the limit of large ripple wavelengths, it approaches the flat surface result from above. On the other hand, when the ripple amplitude is comparable with or larger than the penetration depth, a maximum in the yield function is observed for values of λ , which exceed the ripple amplitude by a numerical factor of $\simeq 6-7$. The deviations of the yield from the flat surface result, $[Y(\lambda) - Y(0)]$, in each case, can be as large as 240%. In the region of

small values of λ and for large values of h_o , the yield is heavily suppressed by the surface roughness. Note that this type of behavior was previously emphasized by Sigmund, who pointed out that the presence of “spike-like” features on the target surfaces, leads to an effective decrease in the sputtered yield and such “spikes” are very stable under the ion bombardment [38].

The normalized sputtering yield, $Y(\lambda)/Y(0)$, dependence on the ripple wavelength, computed for fixed values of the ripple amplitude, $h_o = 5$ nm, and the penetration depth, $a = 5$ nm, is shown in Fig. 6. Different curves in the figure correspond to different values of the incident angle, θ_i . As one can observe, the qualitative behavior of the yield function is similar in all considered cases. In the region of small ripple wavelengths, the yield grows rapidly with λ , with the rate of increase being defined by both the ripple amplitude and the penetration depth. Note that, in the region of small values of λ , the yield can be substantially suppressed, as compared to the flat surface result (see

$\theta = 45^\circ$ and 55° cases). This behavior is observed for large angles of incidence. In general, as the ripple wavelength is varied, the yield can grow by more than 200%. In all considered cases, the yield function demonstrates a maximum at a certain value of λ . The maximum deviations from the flat surface result are observed for $\theta_i = 45^\circ$. For angles of incidence smaller than this value, the peak value grows with decreasing angle of incidence. On the other hand, for large angles of incidence, the peak value decreases in magnitude with θ_i , the smallest increase of $\simeq 60\%$ being observed for $\theta_i = 55^\circ$. In the region of large ripple wavelengths, the yield decreases with λ , approaching asymptotically the flat surface result for a given angle of incidence.

The angular dependence of the yield function for a flat surface, $Y^f(\theta)$, is defined by the projected path of an incident ion in the target material. The theoretical curve shows an increasing behavior over the range of angles from 0° to 90° [20,21]. When a surface is curved, the local curvature becomes a factor which affects the behavior of the yield. Below, we investigate the effect of the local curvature on the angular yield behavior. Fig. 7 shows the normalized yield, $Y(\theta)/Y(\theta = 0^\circ)$, dependence on the primary ion angle of incidence, θ , computed for ripple structures with fixed $\lambda = 200$ nm, and the penetration depth, $a = 5$ nm. Different curves in the figure correspond to different values of the ripple amplitude, h_o . For small angles of incidence, the yield is an increasing function of the incidence angle in all considered cases of h_o . The rate of growth is larger for larger h_o , which is consistent with the arguments based upon the variations of the yield with local angle of incidence [7]. In the case of a flat surface ($h_o = 0$), the growth continues up the maximum considered angle, $\theta = 90^\circ$. This behavior follows from the Sigmund’s theory, where the flat surface approximation was employed [38]. It should be noted, however, that in the region of large angles of incidence ($\theta \geq 70^\circ$), the theory and, hence, our model cannot be considered robust due to the increased probability of reflective collisions, the shadowing and redeposition effects (in the case of rough surfaces). These effects can significantly affect the yield behavior in this region of large incident angles. In fact, decreasing behavior of the

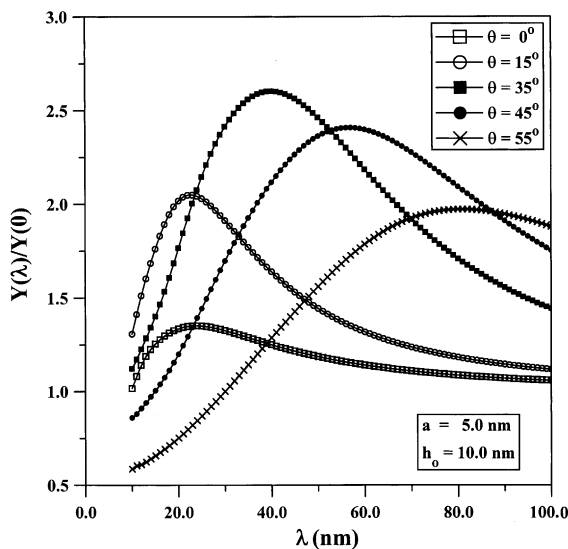


Fig. 6. Normalized yield, $Y(\lambda)/Y(0)$, is plotted as a function of the ripple wavelength, λ , for fixed values of the penetration depth, $a = 5.0$ nm, and the ripple amplitude, $h_o = 10.0$ nm. Different curves in the figure correspond to different values of the incident angles: (1) $\theta = 0^\circ$ (open squares); (2) $\theta = 15^\circ$ (open circles); (3) $\theta = 35^\circ$ (solid squares); (4) $\theta = 45^\circ$; (solid circles); (5) $\theta = 55^\circ$ (crosses). The solid lines are drawn to guide the eye.

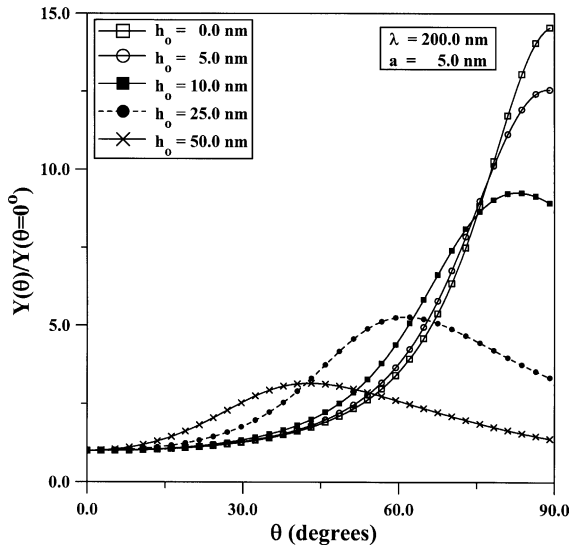


Fig. 7. Normalized yield, $Y(\theta)/Y(\theta=0^\circ)$, is plotted as a function of the angle of incidence, θ , for fixed values of the ripple wavelength, $\lambda = 200.0$ nm, and the penetration depth, $a = 5.0$ nm. Different curves in the figure correspond to different values of the ripple amplitude: (1) $h_o = 0.0$ nm (open squares); (2) $h_o = 5.0$ nm (open circles); (3) $h_o = 10.0$ nm (solid squares); (4) $h_o = 25.0$ nm (solid circles); (5) $h_o = 50.0$ nm (crosses). The solid lines are drawn to guide the eye.

yield function in the regime of large incidence angles is observed even in the case of flat surfaces. In the latter case, this behavior stems from the effects of incident ion reflections and inhibition of the collision cascade development in the bulk of target material by the surface [44]. When the ripple amplitude differs from zero, the qualitative behavior of the angular variations of the yield changes. In this case, the yield increases up to a certain angle, defined by the ripple amplitude and the wavelength, reaches a maximum, and then start to decrease. The value of the angle, at which the yield function have a maximum, shifts with increasing h_o to the region of smaller angles of incidence. We note that, the obtained results are in qualitative agreement with the experimental findings reported by Wittmaack, who studied the incident angle dependence of the sputtering yield for both the target material major constituents and the dopants. It was found that the yield increases with the angle of incidence function, for the major constituents of the target matrix, with the maxi-

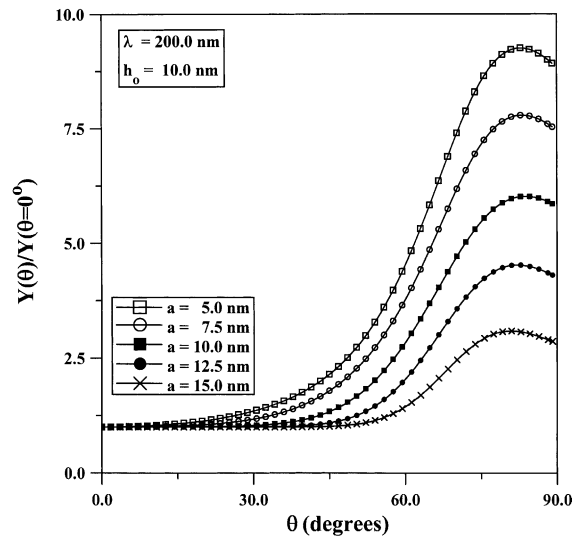


Fig. 8. Normalized yield, $Y(\theta)/Y(\theta=0^\circ)$, is plotted as a function of the angle of incidence, θ , for fixed values of the ripple wavelength, $\lambda = 200.0$ nm, and ripple amplitude, $h_o = 10.0$ nm. Different curves in the figure correspond to different values of the penetration depths: (1) $a = 5.0$ nm (open squares); (2) $a = 7.5$ nm (open circles); (3) $a = 10.0$ nm (solid squares); (4) $a = 12.5$ nm (solid circles); (5) $a = 15.0$ nm (crosses). The solid lines are drawn to guide the eye.

imum value of the deviations from the flat surface result observed for $\theta = 45^\circ$.

In Fig. 8, we show the angular dependence of the normalized yield, $Y(\theta)/Y(\theta=0^\circ)$, computed for the ripple structures with $\lambda = 200$ nm, and the ripple amplitude, $h_o = 10$ nm. Different curves in the figure correspond to different values of the penetration depth. The qualitative behavior of the yield as a function of the incident angle is similar in all considered cases. On the other hand, the absolute values differ significantly, when the penetration depth is varied. In all considered cases, the yield increases with the increasing angle of incidence for small and intermediate values of θ , reaches a maximum and, then, decreases as the angles of incidence approach the grazing incidence limit. For small h_o/a ratio, the yield is not very sensitive to variations in the penetration depth. As the penetration depth exceeds the magnitude of h_o , however, its effect becomes considerable, thus leading to substantial variations in the total yield in the region of large angles of incidence. When the

penetration depth exceeds substantially the ripple amplitude, the yield stabilizes at the value corresponding to the flat surface value. The roughness in this case is not seen from the ion perspective due to small h_o/a ratio.

7. Comparison with experiment

Recent experimental studies of the behavior of the sputtering yields from the rippled surfaces have provided ample results on the various aspects of the problem. The sputtering intensities from the rippled silicon surfaces, eroded by O_2^+ -ions were investigated in [16], employing two different incident ion fluxes of 150 and 15 $\mu\text{A}/\text{cm}^2$. It was found that the intensity function follows closely a linear behavior with the primary ion flux [16]. Thus, our model, where the linear dependence of the sputtering intensities with the ion flux is assumed, is consistent in this respect with the experimental observations. Furthermore, the experimental data, reported in [16], allow for a direct comparison of our theoretical results with experimental data on the sputtering yield behavior during the ripple formation process, i.e. in the course of temporal evolution of the surface morphology. From Fig. 3 of [16], we extracted the experimental points for the normalized yield behavior with sputtered depth, d , for 3, 5, 9 keV O_2^+ -ion sputtering of silicon targets. We note that, following the experimental observations and the results of the BH theory, we assumed that the ripple amplitude, h_o , can be expressed in terms of the sputtered depth as $h = h_i \exp(rd)$,

$$(25)$$

where h_i is the initial surface roughness and r is the growth rate of the ripple amplitude. To convert the ripple amplitude into the sputtered depth, we use Eq. (25), obtaining

$$d = (1/r) \log(h/h_i). \quad (26)$$

Following [16], we use the value of the initial roughness $h_i = 0.25$ nm. The penetration depths and the ripple wavelengths for ripple structures, observed on the O_2^+ -ion eroded silicon matrix surfaces, were taken from Table 1 of [16]. The transition depth, d_T , is the maximum value of the sputtered depth we consider, since the experimen-

tal data provided in [16] indicate that, in the region of $d \geq d_T$, the constant wavelength approximation is not valid anymore. The growth rate, r , was obtained by fitting Eq. (25) to the experimental data [16]. In general, this parameter can be calculated from the BH theory of ripple formation [22]. It should be noted, however, that the growth rates calculated in the framework of this theory are known to underestimate r in the region of small energies and overestimate it, when the ion energies are large. Therefore, we have chosen to use the values of r , obtained in [16] by fitting the exponential function to the experimental data. In Fig. 9, we show the numerical solutions of Eqs. (16)–(19), with the ripple structure parameters reported in [16], along with the experimental data (symbols). As Fig. 9 demonstrates, there is an excellent agreement between the experimental data and our theory, thus showing that our model is capable to provide both qualitative and quantitative description of the sputtering yields from rippled surfaces.

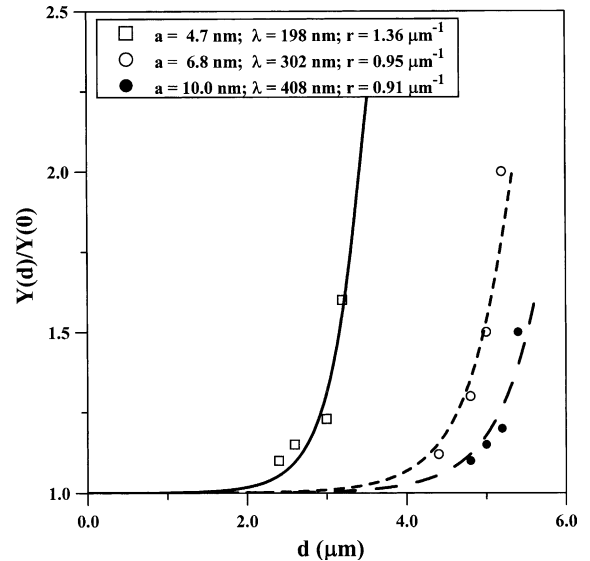


Fig. 9. Normalized yield, $Y(d)/Y(0)$, versus sputtered depth is shown for different values of the incident ion energy and the fixed angle of incidence, $\theta = 40^\circ$. Different curves in the figure correspond to (1) $a = 4.7$ nm, $\lambda = 198.0$ nm, $r = 1.36 \mu\text{m}^{-1}$ (solid line); (2) $a = 6.8$ nm, $\lambda = 302.0$ nm, $r = 0.95 \mu\text{m}^{-1}$ (dotted line); (3) $a = 10.0$ nm, $\lambda = 408.0$ nm, $r = 0.91 \mu\text{m}^{-1}$ (dashed line). The circled, diamonds and triangles correspond to the experimental results, for the same values of the parameters, taken from [16].

The angular dependence of the sputtering yield from the rough pyrolytic and isotropic graphite surfaces, bombarded with 2 keV D^+ -ions at the angles of incidence of 0° , 45° , 70° , 80° , were reported by Kustner et al. [43]. The obtained surface morphologies were studied using STM and the sputter yields were computed via Monte Carlo simulations, performed on model surfaces with the measured distribution of the *local* angles of incidence. It was found that, for small angles of incidence, the surface roughness leads to increased yields, while it suppresses it (substantially, in the case of isotropic graphite), when the angles of incidence are large. The qualitative behavior of the yield as a function of the angle of incidence is very similar to the results obtained in the framework of our model (see Fig. 7). Moreover, Wittmaack studied the angular dependence of the sputtering yields, in experiments with 10 keV O_2^+ -ion bombardment of silicon targets [7]. The experimental data, shown in Fig. 2 of [7], are fully in qualitative agreement with the obtained by us results. Thus, the maximum value of the roughness-induced yield is shown to increase, when the angle of incidence is varied in the range from 35° to 45° , while it decreases rapidly for angles greater than 45° . This behavior is reproduced well in the framework of our model.

While certain features of the yield behavior are well captured in the framework of our model, there exists a number of limitations, which can affect the quantitative conclusions derived from our theory. The limitations stemming from the Sigmund's theory of ion sputtering also apply to our model and have been already discussed in sufficient details in Section 4. The others involve the particular methodology of treatment of the non-planar surfaces in our model and represent the future challenges to the theory. Thus, the effects of shadowing and redeposition, which are not included in our model, may affect the quantitative conclusions obtained in the framework of our theory. While there is no evidence that they are prevalent in the region of incidence angles, where the ripple formation takes place, they are known to substantially modify the yield for large angles of incidence. Moreover, modification of the deposited energy distribution by the sinusoidal target surface profiles are not known. Clearly, more work on both experimental and the-

oretical sides is needed to gain a complete understanding of the corrugated surface effects on the shape of the deposited energy distribution.

8. Summary and conclusions

In conclusion, we have presented a detail account of our model of ion sputtering from surfaces of amorphous materials with ripple morphology. Based upon the Sigmund's theory of ion sputtering, an integral equation describing the sputtering yields from the rippled surfaces was derived. Numerical solutions were obtained to uncover the sputtering yield behavior as a function of the parameters characterizing the ripple morphology of the surfaces and the incident ion beam. In the limiting case of small ripple amplitudes, an analytical form for the yield function was obtained. We found that the surface morphology development may cause substantial variations in the sputtering yields, with the yield magnitude being dependent on a complex interplay between the parameters characterizing both the ripple morphology and the incident ion beam. In particular, we have shown that the yield is an increasing function of the surface roughness, in the initial stages of the ripple structure formation. In this regime, the yield increases with the ripple amplitude approximately following a quadratic law $Y \sim h_o^2$. This form was fitted to experimental data and an excellent agreement was found. In general, we have demonstrated that, depending on the interplay between the surface roughness parameters and the parameters characterizing the primary ion beam, the ripple morphology can both enhance and suppress the yields. While for small h_o/λ ratio, the yield is enhanced, as compared to the flat surface results, it falls-off below the flat surface limit, as the ratio approaches unity. The maximum deviations from the flat surface approximation are observed for h_o/λ ratios close to $1/6$ – $1/7$. We have compared our results with existing experimental data and found that the major conclusions, following from our model, are in an agreement (qualitative and, in some cases, quantitative) with the results obtained in experimental studies. The obtained results are robust for the angles of incidence not exceeding

$\simeq 70^\circ$. For large angles of incidence, the effects of reflective collisions, shadowing and redeposition are expected to affect the *quantitative* conclusions of our model. The ripple formation on amorphous semiconductor surfaces, however, is restricted to angles of incidence not exceeding $\simeq 60^\circ$. Therefore, these effects are not crucial for the considered phenomenon. As we have previously noted (see the preceding article), while we have considered only the case of a single component materials, our model can readily be extended for the multi-component targets.

Acknowledgements

This research was partially supported by the Faculty Research Program at the University of Notre Dame (A.-L. B.).

Appendix A

In this appendix, we provide details of the small ripple amplitude expansion of the set of Eqs. (16)–(19) leading to the analytical form, describing the yield behavior in the initial stages of roughness development. We define the following quantity, which represents the expansion parameter in our model:

$$\omega = \left(\frac{h_o}{a}\right) \left\{ \cos\left(\frac{2\pi x}{\lambda}\right) - \cos\left(\frac{2\pi x_o}{\lambda}\right) \right\}. \quad (\text{A.1})$$

Next, we rewrite Eq. (15), in terms of the new parameter ω , obtaining

$$\begin{aligned} Y = & (F/\bar{\lambda}) \int_0^{\bar{\lambda}} \int_{-\infty}^{\infty} d\bar{x} d\bar{x}_o \Phi(\bar{x}) \exp\left\{-\Gamma_1(\bar{x} - \bar{x}_o)^2\right\} \\ & \times \exp\{-\Gamma_2\omega^2\} \exp\{-\Gamma_3(\bar{x} - \bar{x}_o)\omega\} \\ & \times \exp\{-\Gamma_3(\bar{x} - \bar{x}_o)^2\omega^2\} \\ & \times \exp\{-\Gamma_4(\bar{x} - \bar{x}_o)\} \exp\{-\Gamma_5\omega\}, \end{aligned} \quad (\text{A.2})$$

where $\bar{x} = x/a$ and $\bar{x}_o = x_o/a$ and F is given by Eq. (17). Further, performing the expansion in terms of the small parameter ω and making a simultaneous change of variables $y = \bar{x} - \bar{x}_o$, $x_o = \bar{x}_o$ and $\bar{\lambda} = \lambda/a$, we obtain the following expression for the total yield:

$$\begin{aligned} Y = & \frac{\Lambda n \epsilon a}{(2\pi)\mu\sigma\bar{\lambda}\langle J \rangle} \exp\left\{-\frac{1}{2\epsilon_1^2}\right\} \\ & \times \int_0^{\bar{\lambda}} \int_{-\infty}^{\infty} dx_o dy \Phi(y + x_o) \times \exp\{-\Gamma_1 y^2\} \\ & \times \exp\{-\Gamma_4 y\} [1 - \Gamma_5 \omega + (1/2)\Gamma_5^2 \omega^2 - \Gamma_3 y \omega \\ & + \Gamma_3 \Gamma_5 y \omega^2 + (1/2)\Gamma_3^2 y^2 \omega^2 - \Gamma_2 \omega^2]. \end{aligned} \quad (\text{A.3})$$

The expression (A.3) can be written as a sum of seven integrals

$$\begin{aligned} Y = & \frac{\Lambda n \epsilon a}{(2\pi)\mu\sigma\langle J \rangle \bar{\lambda}} \\ & \times \exp\left\{-\frac{1}{2\epsilon_1^2}\right\} (I_1 + I_2 + I_3 + I_4 + I_5 + I_6 + I_7). \end{aligned} \quad (\text{A.4})$$

The integrals, appearing in Eq. (A.4), are given by

$$\begin{aligned} I_1 = & \int_0^{\bar{\lambda}} \int_{-\infty}^{\infty} dy dx_o \Phi(y + x_o) \exp\{-\Gamma_1 y^2\} \\ & \times \exp\{-\Gamma_4 y\}, \\ I_2 = & -\Gamma_5 \int_0^{\bar{\lambda}} \int_{-\infty}^{\infty} dy dx_o \Phi(y + x_o) \exp\{-\Gamma_1 y^2\} \\ & \times \exp\{-\Gamma_4 y\} \omega, \\ I_3 = & -\Gamma_3 \int_0^{\bar{\lambda}} \int_{-\infty}^{\infty} dy dx_o \Phi(y + x_o) \exp\{-\Gamma_1 y^2\} \\ & \times \exp\{-\Gamma_4 y\} y \omega, \\ I_4 = & \frac{\Gamma_5^2}{2} \int_0^{\bar{\lambda}} \int_{-\infty}^{\infty} dy dx_o \Phi(y + x_o) \exp\{-\Gamma_1 y^2\} \\ & \times \exp\{-\Gamma_4 y\} \omega^2, \\ I_5 = & -\Gamma_2 \int_0^{\bar{\lambda}} \int_{-\infty}^{\infty} dy dx_o \Phi(y + x_o) \exp\{-\Gamma_1 y^2\} \\ & \times \exp\{-\Gamma_4 y\} \omega^2, \\ I_6 = & \Gamma_3 \Gamma_5 \int_0^{\bar{\lambda}} \int_{-\infty}^{\infty} dy dx_o \Phi(y + x_o) \exp\{-\Gamma_1 y^2\} \\ & \times \exp\{-\Gamma_4 y\} y \omega^2, \\ I_7 = & \frac{\Gamma_3^2}{2} \int_0^{\bar{\lambda}} \int_{-\infty}^{\infty} dy dx_o \Phi(y + x_o) \exp\{-\Gamma_1 y^2\} \\ & \times \exp\{-\Gamma_4 y\} y^2 \omega^2. \end{aligned} \quad (\text{A.5})$$

After some simple algebra, we obtain the following expressions for the integrals I_i , $i = (1, 7)$:

$$\begin{aligned}
 I_1 &= \sqrt{\frac{\pi}{\Gamma_1}} \exp \left\{ \frac{\Gamma_4^2}{4\Gamma_1} \right\}, \\
 I_2 &= -\frac{1}{2} \Gamma_5 \tan \theta \frac{2\pi h_o^2}{a^2 \lambda} \sqrt{\frac{\pi}{\Gamma_1}} \exp \left\{ \frac{\Gamma_4^2}{4\Gamma_1} \right\} \\
 &\quad \times \exp \left(- \left(\frac{2\pi}{\lambda} \right)^2 \frac{1}{4\Gamma_1} \right) \sin \left(\frac{\pi \Gamma_4}{\lambda \Gamma_1} \right), \\
 I_3 &= \frac{1}{4} \Gamma_3 \tan \theta \frac{2\pi h_o^2}{a^2 \lambda} \sqrt{\frac{\pi}{\Gamma_1}} \exp \left\{ \frac{\Gamma_4^2}{4\Gamma_1} \right\} \\
 &\quad \times \exp \left(- \left(\frac{2\pi}{\lambda} \right)^2 \frac{1}{4\Gamma_1} \right) \\
 &\quad \times \left(\frac{2\pi}{\lambda \Gamma_1} \cos \left(\frac{\pi \Gamma_4}{\lambda \Gamma_1} \right) + \frac{\Gamma_4}{\Gamma_1} \sin \left(\frac{\pi \Gamma_4}{\lambda \Gamma_1} \right) \right), \\
 I_4 &= \frac{1}{2} \Gamma_5^2 \frac{h_o^2}{a^2} \sqrt{\frac{\pi}{\Gamma_1}} \exp \left\{ \frac{\Gamma_4^2}{4\Gamma_1} \right\} \\
 &\quad \times \left(1 - \cos \left(\frac{\pi \Gamma_4}{\lambda \Gamma_1} \right) \exp \left(- \frac{2\pi^2}{\lambda} \frac{1}{4\Gamma_1} \right) \right), \\
 I_5 &= -\Gamma_2 h_o^2 \sqrt{\frac{\pi}{\Gamma_1}} \exp \left\{ \frac{\Gamma_4^2}{4\Gamma_1} \right\} \\
 &\quad \times \left(1 - \cos \left(\frac{\pi \Gamma_4}{\lambda \Gamma_1} \right) \exp \left(- \left(\frac{2\pi}{\lambda} \right)^2 \frac{1}{4\Gamma_1} \right) \right), \\
 I_6 &= -\frac{1}{2} \Gamma_5 \Gamma_3 h_o^2 \sqrt{\frac{\pi}{\Gamma_1}} \exp \left\{ \frac{\Gamma_4^2}{4\Gamma_1} \right\} \\
 &\quad \times \left(1 - \cos \left(\frac{\pi \Gamma_4}{\lambda \Gamma_1} \right) \frac{\Gamma_4}{\Gamma_1} \exp \left(- \frac{2\pi^2}{\lambda} \frac{1}{4\Gamma_1} \right) \right. \\
 &\quad \left. + \frac{2\pi}{\lambda \Gamma_1} \sin \left(\frac{\pi \Gamma_4}{\lambda \Gamma_1} \right) \exp \left(- \left(\frac{2\pi}{\lambda} \right)^2 \frac{1}{4\Gamma_1} \right) \right), \\
 I_7 &= \frac{1}{4} h_o^2 \Gamma_3^2 \sqrt{\frac{\pi}{\Gamma_1}} \exp \left\{ \frac{\Gamma_4^2}{4\Gamma_1} \right\} \\
 &\quad \times \left[\frac{1}{\Gamma_1} - \sqrt{\frac{\pi}{\Gamma_1}} \left(1 - \left(\frac{2\pi}{\lambda} \right)^2 \frac{1}{2\Gamma_1} \right) \right. \\
 &\quad \times \exp \left\{ - \left(\frac{2\pi}{\lambda} \right)^2 \frac{1}{4\Gamma_1} \right\} \cos \left(\frac{\pi \Gamma_4}{\lambda \Gamma_1} \right) \\
 &\quad + \frac{\Gamma_4}{2\Gamma_1} \frac{2\pi}{\lambda} \exp \left\{ - \frac{2\pi^2}{\lambda} \frac{1}{4\Gamma_1} \right\} \sin \left(\frac{\pi \Gamma_4}{\lambda \Gamma_1} \right) \\
 &\quad \left. + \frac{\Gamma_4}{2\Gamma_1^2} \left[1 - \cos \left(\frac{\pi \Gamma_4}{\lambda \Gamma_1} \right) \exp \left\{ - \left(\frac{2\pi}{\lambda} \right)^2 \frac{1}{4\Gamma_1} \right\} \right] \right].
 \end{aligned} \tag{A.6}$$

Using Eqs. (A.4) and (A.6), it is straightforward to obtain the equation for the yield behavior in the limit of small values of ripple amplitudes h_o and for an arbitrary angle of incidence. The functional form is given by the Eq. (21) in the text. In the case of normal incidence ($\theta = 0^\circ$), the above expressions can readily be reduced to

$$\begin{aligned}
 I_1 &= \frac{\epsilon A n}{(2\pi) \mu \sigma a} \exp \left\{ - \frac{1}{2\epsilon_1^2} \right\} \sqrt{2\pi \epsilon_1^2}, \\
 I_2 &= I_4 = I_5 = I_6 = I_7 = 0, \\
 I_3 &= \frac{\epsilon A n}{(2\pi) \mu \sigma a} \exp \left\{ - \frac{1}{2\epsilon_1^2} \right\} \sqrt{2\pi \epsilon_2^2} \frac{1}{2} \left(\frac{h_o}{a} \right)^2 \\
 &\quad \times \left[\left(\frac{1}{\epsilon_1^4} - \frac{1}{\epsilon_1^2} \right) \left(1 - \exp \left\{ - \frac{(2\pi \epsilon_2)^2}{2(\lambda/a)^2} \right\} \right) \right].
 \end{aligned} \tag{A.7}$$

Combining Eqs. (A.4) and (A.7), the expression for the sputtering yields in the limit $\theta \rightarrow 0$ can readily be obtained. It is given by Eq. (24) in the text.

References

- [1] D.J. Barber, F.C. Frank, M. Moss, J.W. Steeds, I.S.T. Tsong, *J. Mater. Sci.* 8 (1973) 1030.
- [2] F. Vasiliu, I.A. Teodorescu, F. Glodeanu, *J. Mater. Sci.* 10 (1975) 399.
- [3] S.W. MacLaren, J.E. Baker, N.L. Finnegan, C.M. Loxton, *J. Vac. Sci. Technol. A* 10 (1992) 468.
- [4] A. Zalar, *Thin Solid Films* 124 (1985) 223.
- [5] A. Zalar, *J. Vac. Sci. Technol. A* 5 (1987) 2979.
- [6] F.A. Stevie, P.M. Kahora, D.S. Simons, P. Chi, *J. Vac. Sci. Technol. A* 6 (1988) 76.
- [7] K. Wittmaack, *J. Vac. Sci. Technol. A* 8 (1990) 2246.
- [8] S.P. Smith, in: A. Benninghoven, C.A. Evans, K.D. McKeegan, H.A. Storms, H.W. Werner (Eds.), *Secondary Ion Mass Spectroscopy VII*, Wiley, New York, 1990, p. 107.
- [9] E.-H. Cirlin, J.J. Vajo, T.C. Hasenberg, R.J. Hauenstein, *J. Vac. Sci. Technol. A* 8 (1990) 4101.
- [10] E.-H. Cirlin, J.J. Vajo, R.E. Doty, T.C. Hasenberg, *J. Vac. Sci. Technol. A* 9 (1991) 1395.
- [11] A. Karen, K. Okuno, F. Soeda, A. Ishitani, *J. Vac. Sci. Technol. A* 9 (1991) 2247.
- [12] A. Karen, K. Okuno, F. Soeda, A. Ishitani, in: A. Benninghoven, C.A. Evans, K.D. McKeegan, H.A. Storms, H.W. Werner (Eds.), *Secondary Ion Mass Spectroscopy*, Vol. VII, Wiley, New York, 1990, p. 107.
- [13] K. Wittmaack, in: D. Briggs, M.P. Seah (Eds.), *Practical Surface Analysis*, Vol. 2. Ion and Neutral Spectroscopy, Wiley, Chichester, 1992, p. 122.

- [14] E.-H. Cirlin, *Thin Solid Films* 220 (1992) 197.
- [15] A. Karen, Y. Nakagawa, M. Hatada, K. Okuno, F. Soeda, A. Ishitani, *Surf. Interface Anal.* 23 (1995) 506.
- [16] J.J. Vajo, R.E. Doty, E.-H. Cirlin, *J. Vac. Sci. Technol. A* 14 (1996) 2709.
- [17] P.D. Townsend, J.C. Kelly, N.E.W. Hartley, *Ion Implantation, Sputtering and their Applications*, Academic Press, London, 1976.
- [18] R. Behrish (Ed.), *Sputtering by Particle Bombardment*, Vols. I and II, Springer-Verlag, Heidelberg, 1981, 1983.
- [19] W. Eckstein, *Computer Simulation of Ion–Solid Interactions*, Springer Series in Materials Science, Vol. 10, Springer, Berlin, 1991.
- [20] P. Sigmund, *Phys. Rev.* 184 (1969) 383.
- [21] P. Sigmund, R. Behrisch (Ed.), *Sputtering by Particle Bombardment*, Vol. I, Springer, Berlin, 1981.
- [22] R.M. Bradley, J.M.E. Harper, *J. Vac. Sci. Technol. A* 6 (1988) 2390.
- [23] R.M. Bradley, E.-H. Cirlin, *Appl. Phys. Lett.* 68 (1996) 3722.
- [24] G. Carter, *Appl. Phys. Lett.* 71 (1997) 3066.
- [25] M.A. Makeev, A.-L. Barabasi, *Appl. Phys. Lett.* 72 (1998) 906.
- [26] W.W. Mullins, *J. Appl. Phys.* 28 (1957) 333; D.E. Wolf, J. Villain, *Europhys. Lett.* 13 (1990) 389; S. Das Sarma, P.I. Tamborenea, *Phys. Rev. Lett.* 66 (1991) 325.
- [27] C. Herring, *J. Appl. Phys.* 21 (1950) 301.
- [28] T.M. Mayer, E. Chason, A.J. Howard, *J. Appl. Phys.* 76 (1994) 1633.
- [29] G. Carter, V. Vishnyakov, *Phys. Rev. B* 54 (1996) 17647.
- [30] J. Erlebacher, M.J. Aziz, E. Chason, M.B. Sinclair, J.A. Floro, *Phys. Rev. Lett.* 82 (1999) 2330.
- [31] R. Cuerno, A.-L. Barabasi, *Phys. Rev. Lett.* 74 (1995) 4746.
- [32] M.A. Makeev, R. Cuerno, A.-L. Barabasi, *Nucl. Instr. and Meth. B* 197 (2002) 185.
- [33] M.A. Makeev, A.-L. Barabasi, *Appl. Phys. Lett.* 71 (1997) 2800.
- [34] K. Elst, W. Vandervorst, J. Alay, J. Snauwaert, L. Hellemans, *J. Vac. Sci. Technol. A* 11 (1993) 1968.
- [35] K. Elst, W. Vandervorst, *J. Vac. Sci. Technol. A* 12 (1994) 3205.
- [36] H. Shichi, K. Ohnishi, S. Nomura, *Jpn. J. App. Phys.* 30 (1991) L927.
- [37] K.B. Winterbon, *Radiat. Eff.* 13 (1972) 215.
- [38] P. Sigmund, *J. Mater. Sci.* 8 (1973) 1545.
- [39] J.F. Zeigler, J.P. Biersack, U. Littmark, *The Stopping and Ranges of Ions in Solids*, Vol. I, Pergamon, New York, USA, 1986.
- [40] M.A. Makeev, A.-L. Barabasi, *Appl. Phys. Lett.* 73 (1998) 1445.
- [41] M.A. Makeev, A.-L. Barabási, *Nucl. Instr. and Meth. B*, this issue. doi:10.1016/j.nimb.2004.02.027.
- [42] Y. Yamamura, C. Mossner, H. Oechsner, *Radiat. Eff.: Defects Solids* 103 (1987) 25.
- [43] M. Kustner, W. Eckstein, V. Dose, J. Roth, *Nucl. Instr. and Meth. B* 145 (1998) 320.
- [44] H. Oechsner, *J. Appl. Phys.* 8 (1975) 185.